Simulations of Nearshore Particle-Pair Dispersion in Southern California

LEONEL ROMERO

Earth Research Institute, University of California, Santa Barbara, Santa Barbara, California

YUSUKE UCHIYAMA

Department of Civil Engineering, Kobe University, Kobe, Japan

J. CARTER OHLMANN

Earth Research Institute, University of California, Santa Barbara, Santa Barbara, California

JAMES C. MCWILLIAMS

Institute of Geophysics and Planetary Physics, University of California, Los Angeles, Los Angeles, California

DAVID A. SIEGEL

Earth Research Institute, University of California, Santa Barbara, Santa Barbara, California

(Manuscript received 7 January 2013, in final form 12 April 2013)

ABSTRACT

Knowledge of horizontal relative dispersion in nearshore oceans is important for many applications including the transport and fate of pollutants and the dynamics of nearshore ecosystems. Two-particle dispersion statistics are calculated from millions of synthetic particle trajectories from high-resolution numerical simulations of the Southern California Bight. The model horizontal resolution of 250 m allows the investigation of the two-particle dispersion, with an initial pair separation of 500 m. The relative dispersion is characterized with respect to the coastal geometry, bathymetry, eddy kinetic energy, and the relative magnitudes of strain and vorticity. Dispersion is dominated by the submesoscale, not by tides. In general, headlands are more energetic and dispersive than bays. Relative diffusivity estimates are smaller and more anisotropic close to shore. Farther from shore, the relative diffusivity increases and becomes less anisotropic, approaching isotropy ~10 km from the coast. The degree of anisotropy of the relative diffusivity is qualitatively consistent with that for eddy kinetic energy. The total relative diffusivity as a function of pair separation distance R is on average proportional to $R^{5/4}$. Additional Lagrangian experiments at higher horizontal numerical resolution confirmed the robustness of these results. Structures of large vorticity are preferably elongated and aligned with the coastline nearshore, which may limit cross-shelf dispersion. The results provide useful information for the design of subgrid-scale mixing parameterizations as well as quantifying the transport and dispersal of dissolved pollutants and biological propagules.

1. Introduction

Understanding the transport and dispersion of material in nearshore coastal environments is critical for assessing the fate of pollutant events and the connectivity of nearshore biological communities with the open sea (e.g., Fischer et al. 1979; Cowen and Sponaugle 2009; Lentz and Fewings 2012). For geophysical flows, the study of dispersion can be carried out with particles or drifters as well as passive scalars from field observations and numerical simulations. Particle dispersion can be described by the spreading of a local particle patch using single- (absolute dispersion) or multiple-particle trajectories (relative dispersion). Taylor (1922) and Richardson (1926) provided the basis theoretical framework of absolute and relative dispersion, respectively, for isotropic, homogeneous turbulent flows. While absolute dispersion

Corresponding author address: Leonel Romero, 6832 Ellison Hall, Earth Research Institute, University of California, Santa Barbara, Santa Barbara, CA 93106-3060.
E-mail: leromero@eri.ucsb.edu

DOI: 10.1175/JPO-D-13-011.1

gives information about the transport induced by the largest and most energetic scales of the flow, relative dispersion gives the contribution of velocity components from different scales (Boffetta et al. 2008), such as the energy and enstrophy inertial cascade ranges, and provides information about stirring and mixing (Davis 1983, 1991).

Relative dispersion in the ocean is commonly quantified using ensemble averages of the displacement squared between pairs of particles or drifters as a function of time (Davis 1985; Swenson and Niiler 1996; LaCasce and Ohlmann 2003; Ollitrault et al. 2005; LaCasce 2008; Lumpkin and Elipot 2010; Ohlmann et al. 2012). In recent years, relative dispersion has been investigated with finite Lyapunov exponents, which are also used as diagnostic methods to identify Lagrangian coherent structures and barriers of transport (e.g., Boffetta et al. 2001; D'Ovidio et al. 2004; Harrison et al. 2013).

There are several oceanographic studies of relative dispersion from both numerical simulations and drifting buoy observations in the literature. In open ocean conditions, Ollitrault et al. (2005) reported a cubic power–law dependence of the mean square particle separation as function of time from drifter trajectories in the North Atlantic with pair separations between about 10 and 300 km. Lumpkin and Elipot (2010) also found t^3-power-law dependence in the North Atlantic near the Gulf Stream over a wider range of scales between 1 and 500 km. The cubic-power law was reproduced numerically in the North Atlantic by Poje et al. (2010) from realistic numerical simulations with horizontal grid resolution of $1/12°$ for particle separations larger than 10 km. Based on dimensional scaling, the t^3-power law corresponds to an energy inertial range, either three-dimensional forward cascade or, more relevant for large-scale open ocean condition, two-dimensional inverse cascade (LaCasce 2008).

Open ocean relative dispersion analyses often neglect directionality; however, as shown by O'Dwyer et al. (2000) the large-scale dispersion of floats in the ocean interior is generally anisotropic with larger spreading along contours of potential vorticity. Döös et al. (2011) showed both numerically and from drifter data that large-scale dispersion near the ocean surface is anisotropic with larger dispersion in the zonal direction as a result of the beta effect (the variation of the Coriolis parameter with latitude). Coastal flows are both anisotropic and inhomogeneous due in large part to the presence of the coastal boundary. Haza et al. (2008) reported anisotropic dispersion in the Adriatic Sea with power-law behaviors much weaker than Richardson's scaling (i.e., $R^2 \sim t^3$) with $R^2 \sim t^{1.3}$ and $t^{2.0}$ in the zonal and meridional direction, respectively. Their analysis used model particles trajectories with an initial separation of 1 km.

Only few studies of relative dispersion in the ocean at scales smaller than 1 km have been conducted. Schroeder et al. (2012) made field observations of relative dispersion from initial pair separations between 100 and 1000 m. Their observations with initial separations of 100 m were compared with simulated particle trajectories from a relatively coarse model with a resolution of $1/60°$ ($\approx$1.5 km) and consequently found poor agreement between the data and the simulations. Ohlmann et al. (2012) reported relative dispersion measurements from drifters with initial particle separations as small as 5 m within the Santa Barbara Channel. Their results showed exponential behavior of R^2 between 5 and 100 m followed by power-law behavior of $R^2 \sim t^2$ for scales between 100 and 1000 m but they provided no evidence of anisotropic dispersion.

Exponential behavior of R^2 implies that eddies larger than the particle pair separation are responsible for the dispersion and is generally associated with inertial enstrophy cascade (Lin 1972). Morel and Larcheveque (1974) reported exponential dispersion in the atmosphere from an array of balloons tracked over the Southern Hemisphere. In the ocean, LaCasce and Ohlmann (2003) reported exponential dispersion from surface drifter observations in the Gulf of Mexico at scales between 1 and 50 km.

Recent studies of diffusion near coastal boundaries, including the numerical work by Drake and Edwards (2009) at mesoscales and the observations by Nickols et al. (2012) at submesoscales, have reported that cross-shelf diffusivities increase with increasing distance from the shore near the California coast. Drake and Edwards (2009) determined the cross-shelf diffusivity from the moments of the particle clouds and related it to the first mode internal Rossby radius of deformation. Nickols et al. (2012) calculated the cross-shelf diffusivity assuming a logarithmic boundary layer model that was fitted to observations of mean along-shelf currents as function of the distance from the shore. The presence of the boundary in the coastal environment leads to alongshore shear, which enhances lateral dispersion (List et al. 1990). As shown by Bennett (1987), shear dispersion is anisotropic and can lead to cubic dispersion the direction of the mean flow, but it is not due to energy-cascading inertial range scaling as in the turbulent case.

In this study, a statistical analysis of two-particle dispersion was carried out near the coast of Southern California from particle trajectories generated from offline numerical simulations from the Regional Ocean Modeling System (ROMS). The ROMS output included tidal forcing and realistic atmospheric surface fluxes and the horizontal grid resolution of 250 m allows the characterization of relative dispersion with initial particle separation of 500 m within 15 km from the shore. The relative dispersion analysis investigates the roles of coastal geometry (bays versus headlands), bathymetry, distance from the shore, eddy kinetic energy, and the relative magnitudes of strain and vorticity. The importance of submesoscale stirring on relative dispersion is assessed with particle trajectories from ROMS solutions with a horizontal grid resolution of 75 m. The increase in model resolution leads to increased submesoscale activity because of increased frontal instabilities that contribute to the forward cascade of kinetic energy from mesoscale eddies to dissipation at smaller scales (Capet et al. 2008a,b,c).

The paper is organized as follows. Section 2 provides the theoretical framework used to quantify relative dispersion and diffusivity, and section 3 describes the model and methods used for the analysis of the particle trajectories. In section 4, results of the Lagrangian statistics are provided, including various scalings of the relative dispersion and diffusivity. Results are discussed and summarized in sections 5 and 6, respectively.

2. Analytical background

In this section, we provide the mathematical background describing the two-particle dispersion statistics following Babiano et al. (1990) and LaCasce (2008). The trajectory of particle is described by

$$\frac{d\mathbf{x}}{dt} = \mathbf{v}(t) = \mathbf{u}[\mathbf{x}(t), t], \tag{1}$$

where $\mathbf{v}(t)$ is the vector Lagrangian velocity, and $\mathbf{u}[\mathbf{x}(t), t]$ is the Eulerian velocity evaluated at the particle position $\mathbf{x}(t)$ at time t. After integration, Eq. (1) gives the particle trajectory according to

$$\mathbf{x}(t) = \mathbf{x}_o + \int_0^t \mathbf{v}(\tau)\, d\tau, \tag{2}$$

and the absolute particle displacement corresponds to $\mathbf{X}(t) = \mathbf{x}(t) - \mathbf{x}_o$.

Two particles with trajectories $\mathbf{X}_1$ and $\mathbf{X}_2$ initially separated by $\mathbf{R}_o$ will be separated in time according to

$$\mathbf{R}(t, \mathbf{R}_o) = \mathbf{R}_o + \mathbf{X}_1 - \mathbf{X}_2. \tag{3}$$

In terms of the relative velocity vector $\delta\mathbf{v}(t) = d\mathbf{R}(t)/dt$, Eq. (3) becomes

$$\mathbf{R}(t, \mathbf{R}_o) = \mathbf{R}_o + \int_0^t \delta\mathbf{v}(\tau)\, d\tau. \tag{4}$$

The relative dispersion of two particles initially separated by a distance R_o is defined by

$$R^2(t, R_o) = \langle \mathbf{R}(t, \mathbf{R}_o) \cdot \mathbf{R}(t, \mathbf{R}_o) \rangle, \tag{5}$$

where the angle brackets correspond to an ensemble average at time t over all particles.

For anisotropic flows, the relative dispersion is often defined in two dimensions (i, j) as a tensor according to

$$R_{ij}^2(t, R_o) = \langle R_i(t, R_{o_i}) R_j(t, R_{o_j}) \rangle, \tag{6}$$

whose trace is the total relative dispersion $R^2(t, R_o) = R_{11}^2 + R_{22}^2$, corresponding to Eq. (5). The relative diffusivity tensor is defined by

$$\kappa_{ij}(t) = \frac{1}{2}\frac{dR_{ij}^2(t, R_o)}{dt}, \tag{7}$$

which according to Eq. (6) gives

$$\kappa_{ij}(t) = \langle R_i(t, R_{o_i}) \delta v_j(t) \rangle. \tag{8}$$

Here, anisotropy will be defined relative to the shelf orientation and only the diagonal terms of Eqs. (6) and (7) are considered, for example R_{aa}^2 and R_{cc}^2, where the subscripts a and c correspond to the along- and cross-shelf components, respectively, and will be referred to hereafter as R_a^2 and R_c^2.

Substitution of Eq. (3) into Eqs. (6) and (8) yields

$$R_{ij}^2(t, R_o) = R_o^2 + 2\int_0^t \langle R_{o_i} \delta v_j(\tau) \rangle\, d\tau + \int_0^t \int_0^\tau \langle \delta v_i(T) \delta v_j(\tau) \rangle\, dT\, d\tau \tag{9}$$

and

$$\kappa_{ij}(t) = \langle R_{o_i} \delta v_j(t) \rangle + \int_0^t \langle \delta v_i(t) \delta v_j(\tau) \rangle\, d\tau. \tag{10}$$

The correlation of the initial separation vector and the instantaneous relative velocities $\langle R_{o_i} \delta v_j(t) \rangle$ in the above equations are generally neglected under the assumption of stationary and homogenous conditions for the derivation of various asymptotic solutions. For example, at very short time scales when the relative particle velocities are approximately constant, then $R^2 \sim t^2$ (Batchelor 1950).[1] This is often called the ballistic or Batchelor's regime. For very long time scales, the particle velocities become uncorrelated and the integral of the correlation of the relative velocities in Eq. (10) converges, then κ is approximately constant and $R^2 \sim t$ (Babiano et al. 1990). At scales larger than the energy input scale, but smaller than the largest turbulent features within the energy inertial range $R^2 \sim t^3$, corresponding to Richardson's scaling law, and within the enstrophy cascade the scaling by Lin (1972) predicts an exponential growth of $R^2(t)$.

Following the theoretical work by Bennett (1987), assuming a constant turbulent diffusivity over shear current (say in the x direction) $\gamma = dU/dy$ with random velocity fluctuations in the y direction, the relative diffusivity becomes $R_y^2(t) = 4Kt$ and $R_x^2(t) = 4/3\gamma Kt^3$, where K is the diffusivity for stationary and homogeneous turbulence, with a nonzero cross-correlation $\langle R_x R_y \rangle = K\gamma t^2$. Thus, the relative dispersion in the direction of the mean flow grows similarly as in the turbulent case. However, the probability density function of the particle displacements are expected to be Gaussian for shear dispersion and non-Gaussian for the turbulent case (LaCasce 2008).

3. Methods

a. Model

The ROMS is three-dimensional and solves the primitive equations of motion in a rotating coordinate system including the effects of stratification (Shchepetkin and McWilliams 2005). Here, ROMS solutions for the Southern California Bight are used with a horizontal grid resolution of 250 m, including tidal forcing (Buijsman et al. 2012) and realistic atmospheric surface fluxes provided by the Weather Research and Forecasting Model (WRF). The model configuration consists of a series of one-way nested grids with the coarsest and outermost domain L0 for the U.S. West Coast having a horizontal resolution of 5 km with 514×402 grid cells, followed sequentially by L1, L2, and L3 with horizontal resolutions of 1 km, 250 m, and 75 m, respectively. Each domain has 40 (L0, L1, and L2) or 32 (L3) topography-following levels vertically stretched such that grid cell refinement occurs most strongly near the surface and the bottom. The model topography is based on the 30-arc-second resolution global topography/bathymetry grid (SRTM30; Becker et al. 2009) and when available, the 3-arc-second product from the National Oceanic and Atmospheric Administration/National Geophysical Data Center (NOAA/NGDC) coastal relief dataset (http://www.ngdc.noaa.gov/mgg/coastal/crm.html) for the nearshore regions. The minimum water depths are 50, 3, 3, and 1.5 m for the L0, L1, L2, and L3 domains, respectively. Figure 1 shows the two innermost domains L2 and L3, corresponding to the gray and red boxes, respectively, and the dashed lines indicate the locations of the sponge layers, used to absorb the differences in the flow variables between model resolutions. For more details about the model configuration refer to Buijsman et al. (2012) for the L0–L2 domains and Uchiyama et al. (2013, manuscript submitted to *Cont. Shelf Res.*) for the L3 domain. In this study, we focus on the L2 (250 m) configuration solutions for two seasons: 1) fall 2006 and 2) winter 2007/08. Fall 2006 was chosen to correspond with a field campaign off Huntington Beach (Spydell et al. 2009; Clark et al. 2010), and a nearshore diversion of effluent discharge in Santa Monica Bay. Winter 2007/08 was selected because it was a period with relatively large surface waves, a focus of our future work. This study does not include surface wave effects.

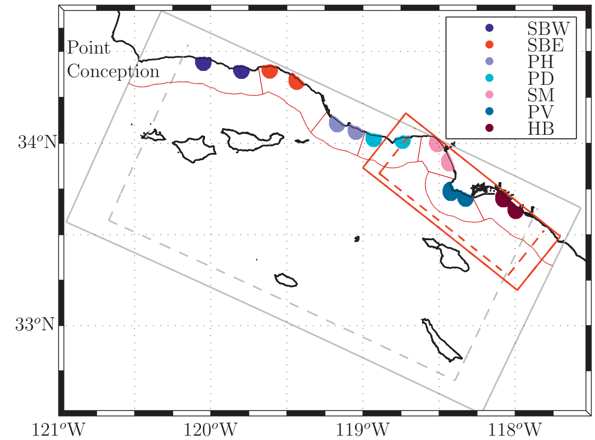

FIG. 1. Particle release locations and model domains. The gray and red boxes show the model domains of the 250- (L2) and 75-m (L3) configurations, respectively, with the dashed lines indicating the sponge layers. The maroon line shows the 15-km offshore band divided up into 7 regions (consult the text for expansions of the acronyms in the legend). Each coastal region contains two release locations color coded as shown in the legend with the red and blue tones corresponding to bays (SBE, SM, and HB) and headlands (SBW, PH, PD, and PV), respectively.

b. Particle tracking

The present study is focused on the relative dispersion of particles within 15 km from the shore from 14

[1] However, for steep wavenumber spectra when the scale of the dominant eddies is larger than the initial pair separation, the relative dispersion at short times is expected to be exponential.

particle release sites (Fig. 1). There are two release sites within each of the regions selected for the analysis, which are labeled as the following: 1) Santa Barbara West (SBW), 2) Santa Barbara East (SBE), 3) Port Hueneme (PH), 4) Point Dume (PD), 5) Santa Monica Bay (SM), 6) Palos Verdes (PV), and 7) Huntington Beach (HB). Each release contained about 1000 particles and was repeated every 12 h. Particles were tracked continuously for up to 5 days or as long as they remained within the domain. The initial array of particles consisted of a circle partially intersecting the coastline with a radius of 5 km, and the particles evenly distributed within the circle with horizontal separation of 250 m. In this study, only pairs of particles with an initial separation of 500 m (±200 m) were considered. All other pairs with smaller and larger separations were excluded from the analysis.

Particle tracking was carried out offline using the three-dimensional flow fields averaged over a period of two hours. All particles were released at 1 m below the surface and were tracked in three dimensions. Only those particles within the top 20 m of water were used for the analysis. Additional experiments were carried out with a maximum depth of 40 m and results were not sensitive to the choice of maximum particle depth. This study is focused on the lateral dispersion near the surface and the vertical dispersion is not considered.

The statistical analysis of the vector quantities used in this study was carried out using a coordinate system relative to the local bathymetry gradient, with the cross-shelf direction aligned with the bathymetric gradient and the along-shelf component at 90° (counterclockwise). A complex vector $\mathbf{u} = u + iv$, with u and v being components in the x and y directions and x being a coordinate along the long axis of the model domain, is decomposed into cross- and along-shelf components according to $u_c = \mathrm{Re}(u\hat{\mathbf{h}}_g^*) = u\hat{h}_x + v\hat{h}_y$ and $u_a = \mathrm{Im}(u\hat{\mathbf{h}}_g^*) = v\hat{h}_x - u\hat{h}_y$, respectively, where $\hat{\mathbf{h}}_g^*$ is the complex conjugate of the bathymetric unit gradient vector $\hat{\mathbf{h}}_g = \hat{h}_x + i\hat{h}_y = \nabla h/|\nabla h|$, with h corresponding to the water depth. Following this convention, the Eulerian velocities and the displacement vectors of particle pairs $\mathbf{R}$ were decomposed into along- and cross-shelf components.

c. Classifying headlands and bays

The release locations, as described above, were selected for the present study based on the energy of the flow, coastal geometry, as well as the bathymetry. Figure 2a shows a map of the eddy kinetic energy at 10-m below the mean sea surface. The eddy kinetic energy, defined as one-half the current variance, is calculated from the

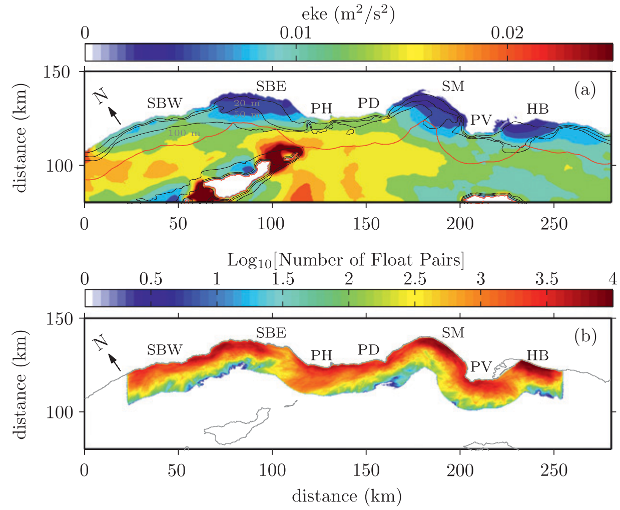

FIG. 2. (a) Eddy kinetic energy map in Cartesian coordinates. The black lines are bathymetric contours at 20, 50, and 100 m. The red line corresponds to a nearshore band 15 km wide. (b) Spatial distribution of the number of particle pairs within 15 km of the coast after 1 day from release. The data correspond to winter 2007/08.

fluctuating velocity flow field without the seasonal mean and trend, which was removed using a Butterworth filter of 3 months. For the SBE, SM, and HB release locations, eddy kinetic energy levels are roughly one-half those found for the other release locations (Fig. 2a). SBE, SM, and HB generally have more pronounced concave-shaped coastlines, weak flows, and shallow bathymetry with weak gradients close to the shore. Based on these distinctions SBE, SM, and HB will be referred to as ''bays,'' and the remainder of release locations will be referred to as ''headlands.'' The red and blue tones used in figures correspond to bays and headland regions, respectively. The data shown in Fig. 2a correspond to winter 2007/08 and are qualitatively similar to results found from fall 2006 (not shown).

d. Particle trajectory analyses

Particle pairs were binned into the seven different regions and into four groups based on their mean position with respect to the distance from the shore L_c at intervals: 0–2, 2–4, 4–6, and 6–15 km. Particles trapped against the coastline with speeds less than 0.25 cm s^{-1} for more than 10 h (roughly 3% of the particles released) were assumed to have ''beached'' and were therefore removed from the analysis. The particles found in the sponge layers were also excluded from analysis.

Figure 3 shows the number of particle pairs as a function of time from release, with each panel corresponding to a different offshore bin. The number of particle pairs is largest close to the shore and at short

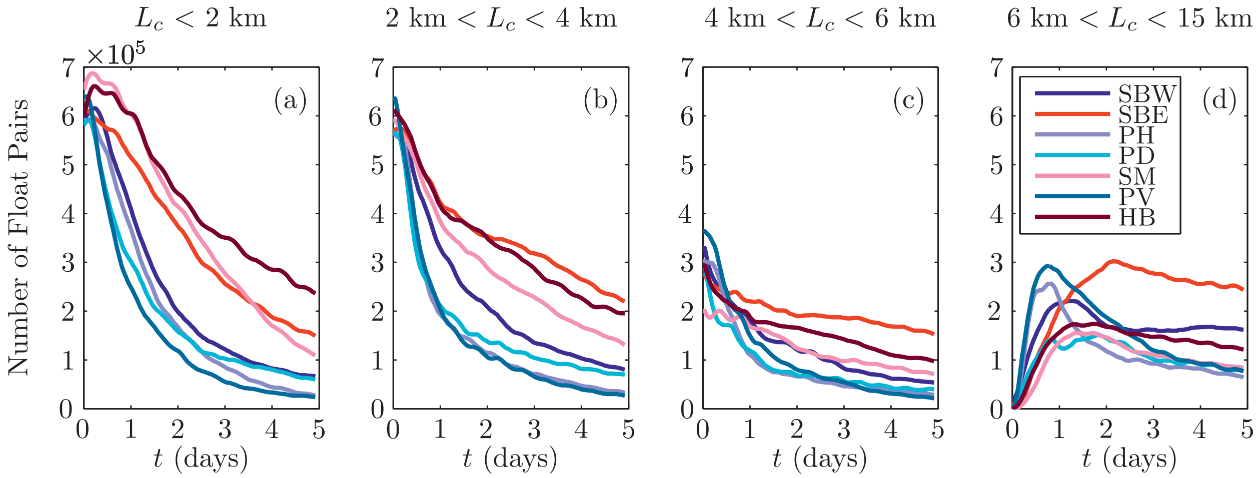

FIG. 3. Number of particle pairs as a function of time, where $t = 0$ corresponds to time of release. (a)–(d) Corresponding different bins ordered with increasing distance from the shore L_c. The data are color coded by regions as indicated in the legend with the red and blue tones corresponding to bays (SBE, SM, and HB) and headlands (SBW, PH, PD, and PV), respectively. The data correspond to winter 2007/08.

times, about 6.5×10^5 pairs. Except for the bin furthest from the shore, the number of pairs tends to decrease very rapidly with time. The data show larger retention of particles close to shore within bays compared to headland areas. The spatial distribution of the number of particle pairs at $t = 1$ day after release for winter 2007/08 data is shown in Fig. 2b. The distribution generally shows larger gradients in the cross-shelf directions indicating preferred particle transport along- over cross-shelf. The spatial and temporal distributions of the number of particles for fall 2006 (not shown) are qualitatively similar to those from winter 2007/08.

Statistics from both seasons (fall 2006 and winter 2007/08 simulations) were combined because both datasets are statistically very similar, increasing the robustness of the statistics presented. As will be shown in section 4a, the variability of the Eulerian statistics between the two datasets is small.

4. Results

a. Eulerian statistics

The Eulerian root-mean-square (rms) velocities are used to characterize the coastal regions and to scale the Lagrangian statistics later in this section. To illustrate the degree of anisotropy of the flow near the coastal boundary, the Eulerian velocities are decomposed into along- and cross-shelf directions using the local bathymetry gradient as described in section 3b. Figures 4a,b show the rms velocity fluctuations plotted as a function of L_c, with $u_{a_{\rm rms}}$ and $u_{c_{\rm rms}}$ corresponding to the along- and cross-shelf components, respectively, which are weighted using the spatiotemporal distribution of particles (e.g., Fig. 2b), thus giving more weight to the regions with more particles. The bars show the variability between fall 2006 and winter 2007/08 simulations, which is generally small, at most 10%.

The rms velocities in the along-shelf direction are either nearly constant or slowly decreasing with L_c, while the cross-shelf components increase with increasing L_c (Figs. 4a,b). Both bays and headlands exhibit anisotropic rms velocities with the largest degree of anisotropy close to shore (Fig. 4c). Values of $u_{a_{\rm rms}}/u_{c_{\rm rms}}$ are approximately 2.5 inshore and decrease to values of ~1.5 at 10-km offshore.

b. Lagrangian statistics

The distributions of the ensemble-mean particle separation squared as a function of time from release are shown in Figs. 5a,b, corresponding to the bins closest and farthest from the shore, respectively. The solid and dashed lines are the components in the along- (i.e., R_a^2) and cross-shelf (i.e., R_c^2) direction, respectively. Both R_a^2 and R_c^2 are larger for headlands than bay areas. Close to shore R_a^2 is greater than R_c^2 for all regions. However at the bin farthest from the shore ($6 < L_c < 15$ km), all curves roughly converge indicating a trend toward isotropy. The R^2 curves approximately exhibit monotonic growth with time, which after 12 h can be approximated by power laws with exponents varying between 1 and 3.

The R^2 errors are small, around 2% or less, except for the cross-shelf component in the bin closest to shore and $t > 3$ days when the uncertainty approaches 10%. The

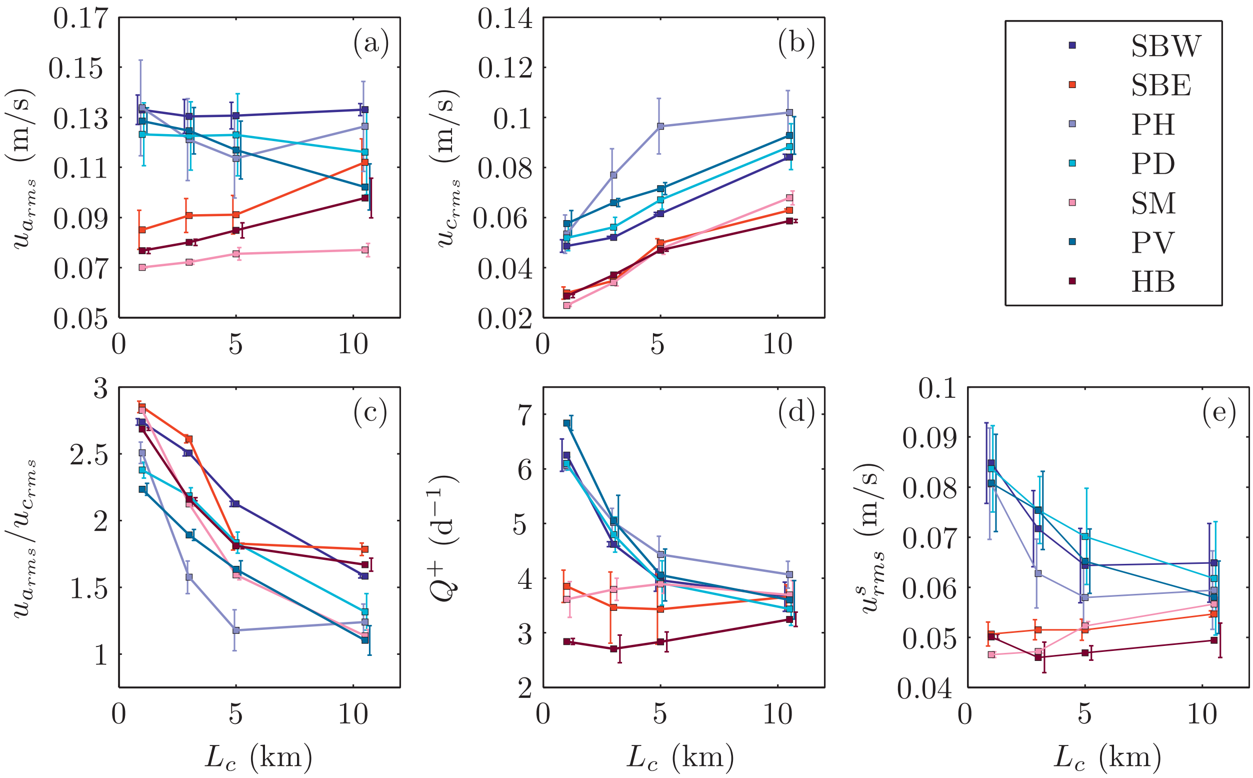

FIG. 4. (a),(b) The rms velocity fluctuations in the along- and cross-shelf directions, respectively, as a function of the distance from the shore L_c. (c),(d) The ratio $u_{a_{\rm rms}}/u_{c_{\rm rms}}$ and the time scale Q^+ against L_c, respectively, where Q^+ is the frequency given by the square root of the Okubo–Weiss parameter averaged over regions dominated by strain. (e) The submesoscale rms currents against L_c are shown. The bars show the variability between fall 2006 and winter 2007/08. The submesoscale flow was obtained from the total 250-m resolution flow field at 10-m below the surface as follows. Let the total flow without the seasonal trend and mean be decomposed by $u = u_m + u_t + u_s$, where u_m is the mesoscale flow, u_t is the flow due to tides, and u_s is the submesoscale flow. Here, u_m is calculated from u by smoothing it in space with an isotropic Gaussian filter with a decorrelation length of 10 km. Then, u_t is approximated from $u - u_m$ band passed between ⅓ and 1½ days. Finally u_s is calculated from $u_s = u - u_m - u_t$.

uncertainties of $R^2(t)$ were calculated by the standard error of the mean with the number of degrees of freedom $N_f = N\Delta t/T_L$, where N is the number of individual particles, $\Delta t = 1$ h is the time resolution of the particle trajectories, and T_L is the e-folding time scale of the Lagrangian autocorrelation.

Prior to calculating the relative diffusivities according to Eq. (7), the R^2 curves were bin averaged with an interval of 6 h to reduce high-frequency variations. Figures 5c,d show the relative diffusivities κ_a and κ_c in the along- and cross-shelf directions, respectively. Similar to the R^2 curves, the relative diffusivities are also anisotropic nearshore (Fig. 5c), while tending toward isotropy offshore (Fig. 5d). The diffusivity curves generally show increasing trends with increasing time for $t < 2$ days. At longer time scales some of the curves approach a nearly asymptotic value and/or are followed by steeper growth with increasing time, which could be an indication of a transition into different relative dispersion regimes, such as increased dispersion because of large-scale strain (i.e., exponential dispersion) or a transition from relative to absolute dispersion with particle separations larger that the local dominant eddies (LaCasce 2008). However, the late time behaviors may be partly artifacts resulting from under sampling.

c. Dispersive velocity and time scale

Two-dimensional turbulent flows are composed of a mixture of cascading turbulence and isolated vortices (McWilliams 1984), which are commonly characterized as regions dominated by deformation and vorticity, respectively. The Okubo–Weiss parameter, $Q = S^2 - \zeta^2$, quantifies the relative magnitudes of strain and vorticity, where $S^2 = S_n^2 + S_s^2$ is the total straining rate squared, with $S_n = u_x - v_y$ and $S_s = u_y + v_x$ being the normal and shear components, respectively, and $\zeta = v_x - u_y$ is the vertical component of vorticity (Okubo 1970; Weiss

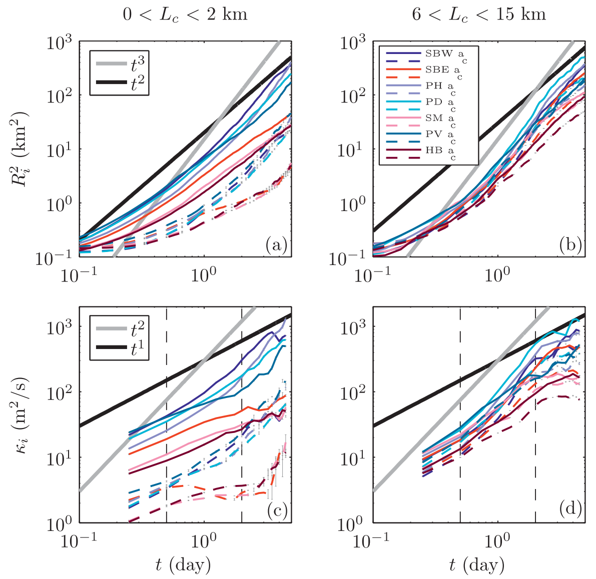

FIG. 5. (a),(b) Mean particle-pair separation squared R_i^2 and (c),(d) relative diffusivity κ_i as a function of time. The colored solid and dashed lines are the along- ($i = a$) and cross-shelf ($i = c$) components, respectively. The bins closest to shore ($L_c < 2$ km) are shown in (a),(c), and those farthest from the shore ($6 < L_c < 15$ km) are shown in (b),(d). The gray and black lines show reference power laws corresponding to $R^2 \sim t^3$ ($\kappa \sim t^2$) and $R^2 \sim t^2$ ($\kappa \sim t$), respectively. The statistics were calculated from particle trajectories from both seasons: fall 2006 and winter 2007/08. The bars show the uncertainty based on the standard error of the mean.

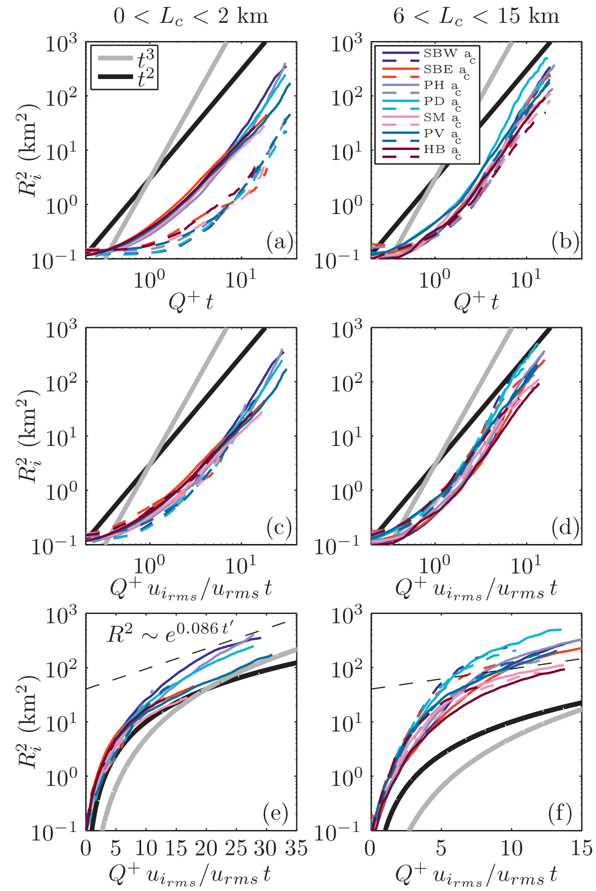

FIG. 6. (a),(b) The R_i^2 curves from Figs. 5a,b with the time axis scaled by Q^+, with the colored solid and dashed lines corresponding to the along- ($i = a$) and cross-shelf ($i = c$) components, respectively. (c)–(f) The time axis is scaled by the anisotropic frequency $Q^+ u_{i_{\rm rms}}/u_{\rm rms}$, with the data shown in log–log and semi-log axes, respectively. The data from (a),(c),(e) correspond to particle pairs with center positions within 2 km offshore, and (b),(d),(f) are pairs between 6 and 15 km from the shore. The black and gray lines are reference power laws of t^2 and t^3, respectively. The black-dashed line in (e),(f) is a reference exponential curve proportional to $\exp(0.086 Q^+ u_{i_{\rm rms}}/u_{\rm rms} t)$.

1991). An important parameter for dispersion is Q because areas of positive Q values correspond to hyperbolic regions, which are dispersive, while negative values are generally eddy cores with little dispersion (Waugh et al. 2006; Poje et al. 2010). As shown numerically by Poje et al. (2010), both Q and relative dispersion are enhanced at small scales, particularly for model resolutions below 1 km. Poje et al. (2010) proposed a modified Okubo–Weiss parameter $1/Q^+$ as the characteristic time scale for dispersion at short times, where Q^+ is the average of $Q^{1/2}$ over areas dominated by strain ($Q > 0$). Their numerical results show that by scaling the time by Q^+, the dispersion curves $R^2(tQ^+)$ collapsed across five different model resolutions.

In this study, we investigate the applicability of Q^+ for characterizing the dispersion across the different coastal regions determining $Q^+ = \langle\sqrt{Q}\rangle$, for $Q > 0$, with the angle brackets corresponding to a spatiotemporal average using the particle location histograms as scaling weights. In Fig. 4d, Q^+ is plotted as a function of L_c showing that headlands, especially inshore, have larger strain rates than embayments. While Q^+ is nearly constant as a function of offshore distance for bays, headlands show a decreasing trend with increasing L_c, approximately converging with bays at the farthest offshore bin. The enhancement of Q^+ toward the shore near headlands may be associated with enhanced boundary shear and submesoscale eddies.

Figures 6a,b show the mean particle separation squared as a function of time with the time axis scaled by Q^+. The $R^2(Q^+t)$ curves collapse into two groups, along and cross shelf, for the inner-shelf case, while both components converge far from the shore. This implies that at short times, the dispersion is controlled by the hyperbolicity of flow across the different regions. We then scale the time axes by the rms velocities normalized by rms speed. Figures 6c,d show $R_a^2(Q^+u_{a_{\rm rms}}/u_{\rm rms}t)$ and $R_c^2(Q^+u_{c_{\rm rms}}/u_{\rm rms}t)$ approximately collapsing the data

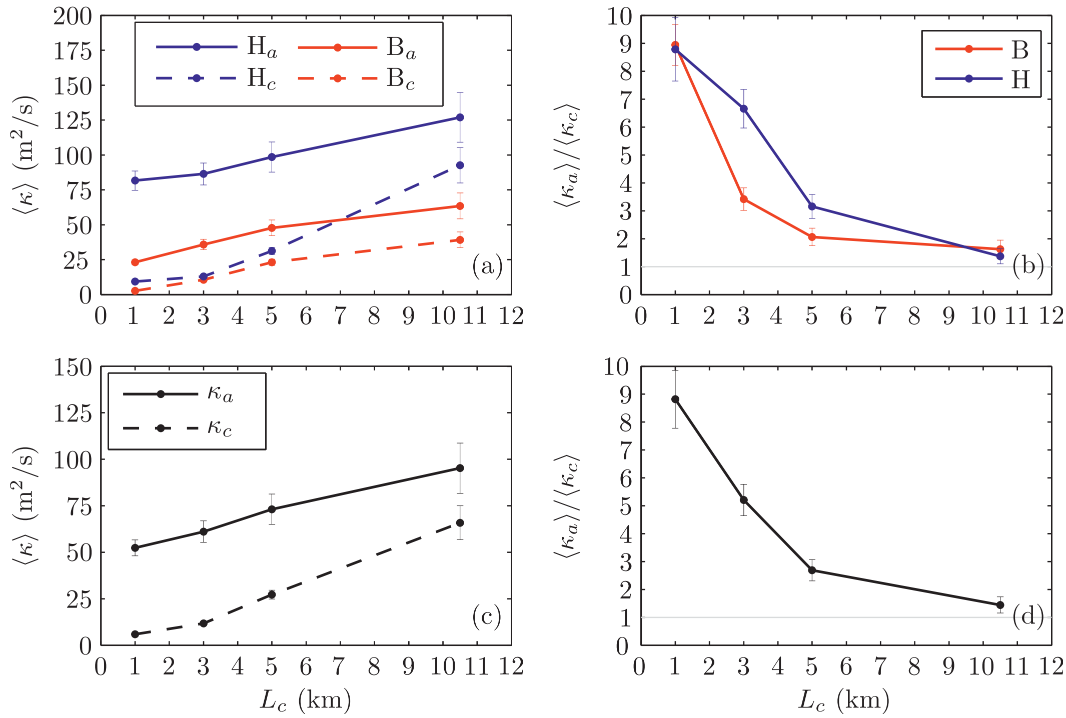

FIG. 7. Composite averages of the mean relative diffusivities between ½ and 2 days. (a),(b) The red and blue lines correspond to bays and headlands, respectively. (c),(d) Composite averages of all the data combined are shown. The solid and dashed lines in (a),(c) show the average diffusivities in the along- and cross-shelf directions, respectively. The degree of anisotropy $\langle\kappa_a\rangle/\langle\kappa_c\rangle$ against L_c is shown in (b),(d). The bars show the standard error of the mean.

regardless of direction. However, notice that Fig. 6d collapses the data less well than Fig. 6b, which implies that the directional scaling relative to the shelf is less effective far from the shore. Thus, the Eulerian velocities and mean strain can effectively scale the relative dispersion in the nearshore waters with anisotropic time scales $u_{\mathrm{rms}}/Q^+u_{a_{\mathrm{rms}}}$ and $u_{\mathrm{rms}}/Q^+u_{c_{\mathrm{rms}}}$.

d. Mean relative diffusivity

The relative diffusivities are temporally averaged and combined across multiple regions into composite sets to best illustrate their dependence on direction, distance offshore, and coastal topology. Figures 5c,d show that headlands have larger relative diffusivities than that of bays, particularly close to shore. The relative diffusivities monotonically increase for $½ < t < 2$ days except for the cross-shelf component in SBE.

Average relative diffusivities are calculated over the interval from ½ to 2 days and analyzed with respect to L_c. Figure 7a shows the mean relative diffusivities $\langle\kappa_i\rangle$ with the solid and dashed lines corresponding to the along- ($i = a$) and cross-shelf ($i = c$) components, respectively. Figure 7b shows the degree of anisotropy $\langle\kappa_a\rangle/\langle\kappa_c\rangle$ as a function of L_c. The red and blue lines correspond to composite averages of the bays and headlands, respectively. Composite sets combining both bays and headland regions of the average relative diffusivities and degree of anisotropy are shown in Figs. 7c,d, respectively. The mean relative diffusivities show an increasing trend with increasing L_c and are always larger for headlands than bays. The degree of anisotropy is largest close to shore and decreases with increasing L_c, approaching 1 at about 10 km from the shore. This trend is similar for both bays and headlands.

The average relative diffusivities between ½ and 2 days $\langle\kappa_a\rangle$ and $\langle\kappa_c\rangle$ are plotted against the rms velocities in Figs. 8a,c, respectively. The rms velocities are better correlated with the average diffusivities in the cross-shelf direction. Based on the average ratio of the diffusivities to the rms velocities, the scalings imply diffusion length scales of just 800 and 500 m in the along- and cross-shelf directions, respectively, which correspond to small submesoscale values. Figures 8b,d show the average diffusivities $\langle\kappa_a\rangle$ and $\langle\kappa_c\rangle$ against dimensionally consistent scalings $u^2_{a_{\mathrm{rms}}}Q^{+(-1)}$ and $u^2_{c_{\mathrm{rms}}}Q^{+(-1)}$, respectively. This scaling is close in magnitude to the data, and gives slightly improved correlations over the scaling based on the rms velocities. The time scale given by $1/Q^+$, as shown in Fig. 4d, varies between 3.5 and 8 h, also corresponding to the submesoscale. None of the

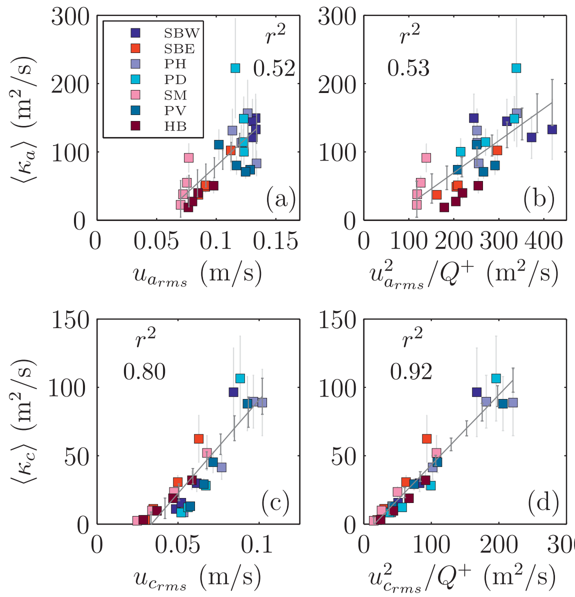

FIG. 8. Bin-averaged relative diffusivities (a),(b) $\langle\kappa_a\rangle$ and (c),(d) $\langle\kappa_c\rangle$ against various Eulerian scalings. The brackets correspond to an average between ½ and 2 days. The relative diffusivities are plotted against the corresponding rms velocity components in (a),(c). The $\langle\kappa_a\rangle$ and $\langle\kappa_c\rangle$ vs $u^2_{a_{\mathrm{rms}}}/Q^+$ and $u^2_{c_{\mathrm{rms}}}/Q^+$, respectively, are shown in (b),(d). The bars correspond to the standard error to the mean. The solid lines are linear regressions with 95% confidence intervals.

along-shelf relative diffusivity scalings provide correlations with r^2 values greater than 0.5. However, the cross-self diffusivity scalings have r^2 values $\geq$0.8. Figures 8b,d represent our best complete scalings (i.e., they have the right dimensions), if only marginally. Additional scaling analyses of the relative diffusivity were considered using the rms velocities and a length scale, such as the cross-shore distance, water depth, etc.; however, those scalings consistently yielded poor correlations for the along-shelf component and similarly good correlations for the cross-shelf component compared to the other scalings considered.

The average diffusivity and its relationship to the rms velocity or variance through constant length scales or time scales, respectively, are only valid in the asymptotic limit for long time scales within an absolute dispersion regime (Swenson and Niiler 1996). The scalings of the average diffusivity between ½ and 2 days introduced in this section are not necessarily valid for other time intervals.

e. Power-law modeling of pair separation statistics

To model the anisotropic diffusivities, we construct an analytical model of the relative dispersion. Motivated by the collapse of the $R_a^2(Q^+u_{a_{\mathrm{rms}}}/u_{\mathrm{rms}}t)$ and $R_c^2(Q^+u_{c_{\mathrm{rms}}}/u_{\mathrm{rms}}t)$ curves in Figs. 6c,d, the dispersion curves for ¼ $< t <$ 4 days are fitted to the following power-law models:

$$R_a^2 = A_a(Q^+u_{a_{\mathrm{rms}}}/u_{\mathrm{rms}}t)^{B_a} \quad (11)$$

and

$$R_c^2 = A_c(Q^+u_{c_{\mathrm{rms}}}/u_{\mathrm{rms}}t)^{B_c}\,. \quad (12)$$

The time interval was chosen based on the monotonic behavior observed in Figs. 5a,b, and the results are not particularly sensitive to small changes to the time interval. The best-fit coefficients were combined in two groups: bays and headland regions. The best-fit B_a and B_c, shown in Figs. 9a,b, respectively, are well correlated with L_c, with B_a nearly converging with B_c at $L_c = 10$ km. Regardless of direction, B_a and B_c are larger for headlands than bay areas. Here, B_a varies between 2 and 2.5 for headlands and for bays between 1.5 and 2.2, while B_c increases from 1.8 to 2.5 for headlands and from 1 to 2.2 for bays. Linear fits of B_a and B_c versus L_c yield the following for bays:

$$B_a = 6.7\times10^{-5}\ (\mathrm{m}^{-1})L_c + 1.68 \pm 0.12 \quad \text{and} \quad (13)$$

$$B_c = 1.2\times10^{-4}\ (\mathrm{m}^{-1})L_c + 1.05 \pm 0.16\,, \quad (14)$$

and the following for headlands:

$$B_a = 5.2\times10^{-5}\ (\mathrm{m}^{-1})L_c + 2.07 \pm 0.16 \quad \text{and} \quad (15)$$

$$B_c = 8.2\times10^{-5}\ (\mathrm{m}^{-1})L_c + 1.66 \pm 0.17\,, \quad (16)$$

with 95% confidence intervals.

Based on dimensional grounds, the best-fit scaling factors A_a and A_c are plotted as a function of $(u_{\mathrm{rms}}/Q^+)^2$ in Figs. 9c,d, respectively. The coefficients A_a increase weakly with increasing $(u_{\mathrm{rms}}/Q^+)^2$; while A_c increases more rapidly with increasing $(u_{\mathrm{rms}}/Q^+)^2$. Linear fits of A_a versus $(u_{\mathrm{rms}}/Q^+)^2$ with 95% confidence intervals in units of squared meters for both bays and headlands yield

$$A_a = 1.2\times10^{-2}(u_{\mathrm{rms}}/Q^+)^2 + 2.1\times10^5 \pm 5.8\times10^4\,, \quad (17)$$

while A_c versus $(u_{\mathrm{rms}}/Q^+)^2$ for bays give

$$A_c = 6.0\times10^{-2}(u_{\mathrm{rms}}/Q^+)^2 + 2.7\times10^5 \pm 1.4\times10^5\,, \quad (18)$$

and for headlands

$$A_c = 3.5\times10^{-2}(u_{\mathrm{rms}}/Q^+)^2 + 1.6\times10^5 \pm 1.1\times10^5\,. \quad (19)$$

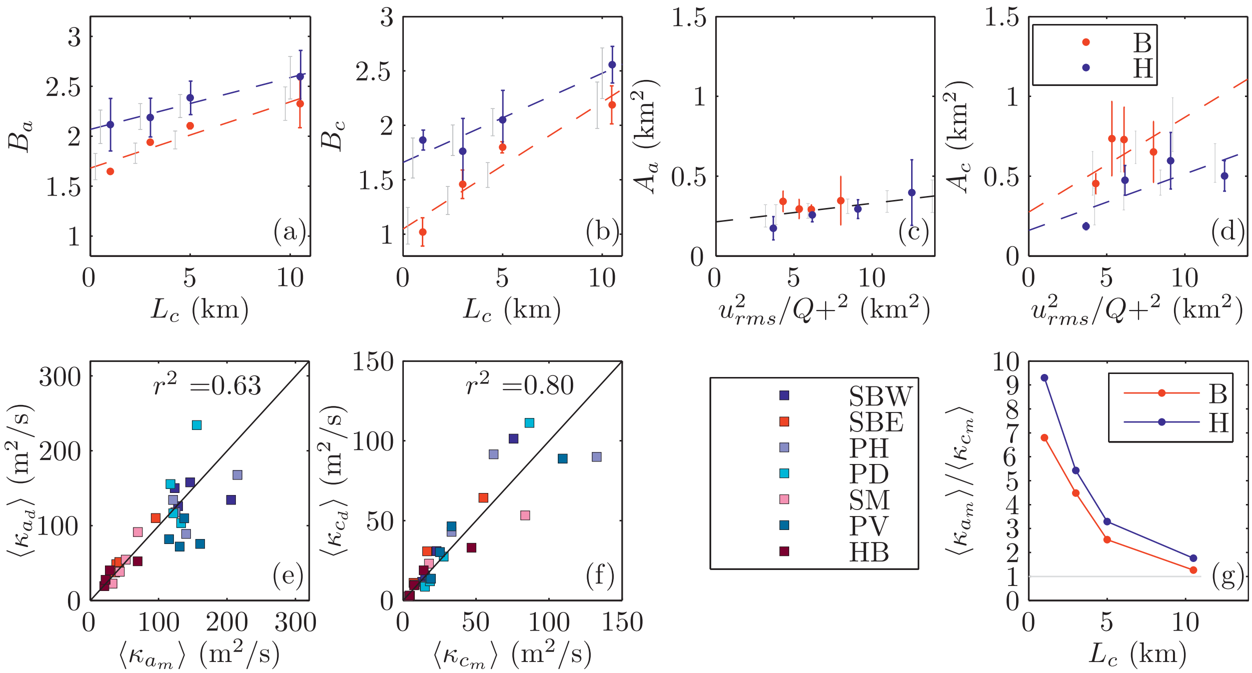

FIG. 9. The best-fit coefficients (a) B_a, (b) B_c, (c) A_a, and (d) A_c are shown from Eqs. (11) to (12) plotted as function of the distance from the shore L_c. The red and blue circles correspond to composite averages for bays and headlands, respectively. The dashed lines show the best fit. (e),(f) The average diffusivities between ½ and 2 days calculated from the data and the power-law model with the best-fit coefficients in Eqs. (13)–(19). (g) Composite averages for bays and headlands of the predicted degree of anisotropy as a function of L_c (cf. Fig. 7b).

According to Eqs. (11) and (12), the weak dependence of A_a on $(u_{\rm rms}/Q^+)^2$ compared to that of A_c implies that the dispersion in the along-shelf direction will be more strongly related to Q^+ compared to the cross-shelf direction.

To test the predictive ability, the power-law models in Eqs. (11) and (12) combined with Eqs. (13)–(19) are used to calculate the average diffusivity between ½ and 2 days and compared with the Lagrangian data. Figures 9e,f show the average relative diffusivities in the along- and cross-shelf directions, respectively. The power-law model accounts for 63% and 80% of the variance in the along- and cross-shelf directions, respectively. There is a substantial improvement in the predictive skill for the along-shelf diffusivity compared to the scaling results shown in Fig. 8. The predicted degree of anisotropy of bays and headlands shown in Fig. 9g is qualitatively similar to that from the data in Fig. 7c, but it is generally underestimated close to shore for bay areas.

f. Scale-dependent relative diffusivity

The dependence of the two-particle diffusivities on scale, or rms separation, is shown in Fig. 10, where the along- and cross-shelf components correspond to Figs. 10a,c and 10b,d, respectively, with the headland data shown in the top panels and the bay data shown in the bottom panels. All the curves generally exhibit monotonically increasing behavior with increasing separation distance and are often followed by a roll off and/or a sharp increasing trend. The relative dispersion as a function of rms separation is larger for headland regions than bays. The along-shelf component of headlands exhibits the least scatter, while the cross-shelf component in bays shows the most variability. There is also considerable variability across the different regions, and the relative diffusivity in the along-shelf direction is generally larger than that in the cross-shelf direction.

The scatter and variability of the diffusivity versus particle pair separation can be partially removed by nondimensionalizing the variables with time scales $u_{\rm rms}u_{i_{\rm rms}}^{-1}Q^{+(-1)}$ and length scales $A_i^{1/2}$ ($i = a, c$) as given by

$$\kappa_i' = \kappa_i A_i^{-1} Q^{+(-1)} u_{\rm rms} u_{i_{\rm rms}}^{-1} \tag{20}$$

and

$$R_i' = R_i / A_i^{1/2}, \tag{21}$$

where the rms particle separation $R_i = (R_i^2)^{1/2}$, and A_i corresponds to the best fits obtained in Eqs. (17)–(19). Figures 11a,c and 11b,d show κ_a' against R_a' and κ_c'

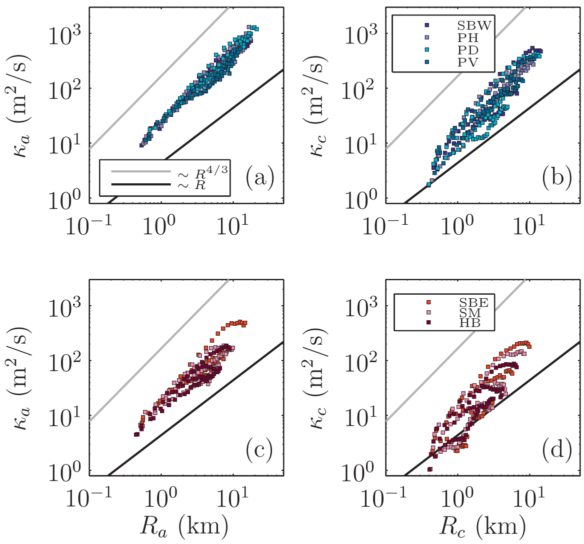

FIG. 10. Relative diffusivity components κ_a and κ_c plotted against the rms particle pair separation components R_a and R_c, respectively. The subscripts a and c refer to the along- and cross-shelf components, respectively. The data from (a),(b) are for headlands and (c),(d) are for bays. The thick black and gray lines are reference power-laws R ($\kappa \sim t$) and $R^{4/3}$ ($\kappa \sim t^2$), respectively.

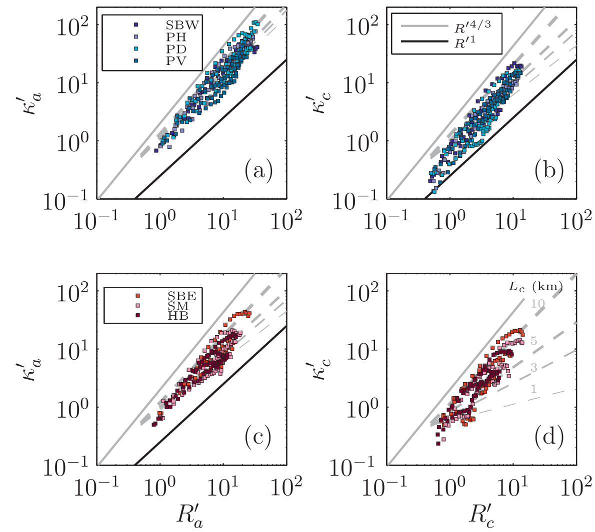

FIG. 11. Nondimensional relative diffusivity components (a),(c) κ'_a and (b),(d) κ'_c [Eq. (20)] plotted against the nondimensional rms particle pair separation components R'_a and R'_c [Eq. (21)], respectively. The subscripts a and c refer to the along- and cross-shelf components, respectively. The dashed-gray lines correspond to the best power-law fits from Eqs. (13) to (19), with the line thickness increasing with increasing distance from the shore as indicated in (d). The thick black and gray lines are the reference power-law R ($\kappa \sim t$) and $R^{4/3}$ ($\kappa \sim t^2$), respectively.

against R'_c, respectively, including the predicted curves, which are shown with gray-dashed lines with parametric dependence on L_c. The analytical predictions are based on power-law models Eqs. (11) and (12) nondimensionalized through Eq. (21) and combined with Eq. (7) yielding

$$\kappa'_i = \frac{B_i}{2} R'^{2(B_i - 1)/B_i}, \tag{22}$$

with B_i corresponding to the best fits in Eqs. (13)–(16). The predictions are in close agreement with the data and show that the large variability of the nondimensional relative diffusivity within bays, particularly for the cross-shelf component, is due to changes of B_i with L_c.

g. Exponential regime

As discussed in section 4b, the $R^2(t)$ and $\kappa(t)$ curves occasionally exhibit sudden increased dispersal and diffusivity at long times ($t > 3$ days). This is qualitatively consistent with the drifter observations by List et al. (1990) near the coast of Southern California who reported sudden increased dispersion after 1 day at scales from 3 to 4 km. Figures 6e,f show $R_a^2(Q^+ u_{a_{\rm rms}}/u_{\rm rms} t)$ and $R_c^2(Q^+ u_{c_{\rm rms}}/u_{\rm rms} t)$, respectively, with semilogarithmic axes. Also shown is a black-dashed reference line proportional to $\exp(0.086t')$, with $t' = Q^+ u_{c_{\rm rms}}/u_{\rm rms} t$. There is a general tendency, particularly for the along-shelf component, for the scaled separation distances squared to become approximately proportional to $\exp(0.086t')$ for large times. Thus, the mean-squared separation can be approximated for large time scales by

$$R_i^2 = R_e^2 \exp(c' t'), \tag{23}$$

with R_e corresponding to the scale at which the exponential dispersion is effective and $c' \approx 0.086$ is a dimensionless constant. Based on Eq. (23), the relative dispersion can be obtained through Eq. (7). After eliminating the time dependence gives

$$\kappa_i = \frac{c'}{2} Q^+ \frac{u_{i_{\rm rms}}}{u_{\rm rms}} R_i^2. \tag{24}$$

Figure 12 shows $\kappa_i(u_{\rm rms}/Q^+ u_{i_{\rm rms}})$ against R_i with the along- and cross-shelf components in Figs. 12a,c and 12b,d, respectively; the headland data are shown in the top panels and the bay data in the bottom. The Lagrangian data are compared with $(c'/2)R_i^2$, where $c' = 0.086$, which generally serves as a lower bound (meaning that the data is generally above the dashed line) for scales between 3 and 20 km. The late time dispersion is not inconsistent with an exponential mesoscale regime, but it is not well confirmed.

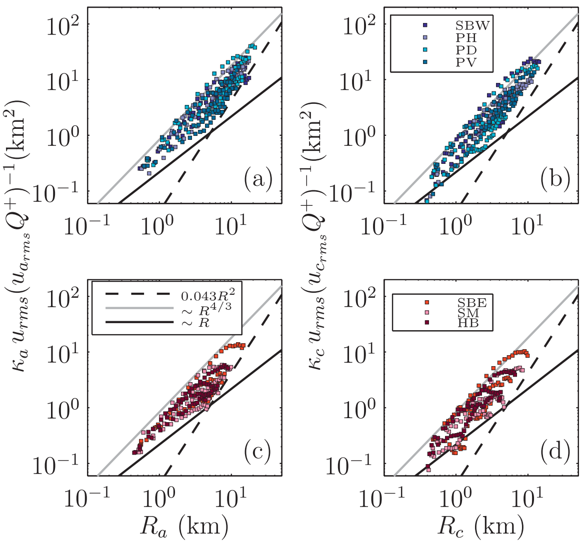

FIG. 12. Normalized relative diffusivity components (a),(c) κ_a and (b),(d) κ_c plotted against the rms particle pair separation components R_a and R_c, respectively. The data from (a),(b) are for headlands and (c),(d) are for bays. The solid black and gray lines are reference power-laws R ($\kappa \sim t$) and $R^{4/3}$ ($\kappa \sim t^2$), respectively. The black-dashed line corresponds to 0.043 R^2.

5. Discussion

The effect of submesoscale on horizontal dispersion is investigated through the characterization of submesoscale activity with respect to the coastal geometry, distance from the shore, and its relationship to Q^+. This is further investigated by extending the Lagrangian analysis to a nested solution with a horizontal resolution of 75 m, which also allows testing the sensitivity of the results to the initial pair separation. As will be shown, the relative dispersion analysis with the 75-m grid also improves the comparison between our results and available surface drifter observations. This section concludes by showing that filaments of large vorticity are preferably aligned with the coastline close to the shore and thus may lead to reduced cross-shelf transport and dispersion within the inner shelf.

a. *Model resolution and submesoscale dynamics*

The simulated coastal circulation in Southern California is primarily forced by mesoscale eddies (10 km or larger), tides, and winds, all of which can drive submesoscale flows. Winds parallel to the coast can give rise to upwelling fronts and jets, which can also generate submesoscale filaments, fronts, and vortices. Straining by mesoscale eddies can generate submesoscale fronts that often become unstable and break into eddies (Flament et al. 1985; Washburn and Armi 1988; Capet et al. 2008a). Tidally induced flows around islands and headlands are known to generate submesoscale eddies in the form of wakes (e.g., Dong and McWilliams 2007; Bassin et al. 2005; Signell and Geyer 1991). In particular, submesoscale vortices induced by tidal flow around headlands have been shown to enhance dispersion by straining (Signell and Geyer 1990). However, as shown by McWilliams (2009), submesoscale coherent vortices are not only generated near headlands but may also be generated within bays, as a result of bay-scale shear close to the shore. As discussed in terms of scalar diffusion by Uchiyama et al. (2013, manuscript submitted to *Cont. Shelf Res.*) dispersion is dominated by submesoscales, not by tides. Visual examination of particle clouds from this study also shows that the particles are spread apart mainly because of small eddies induced by large-scale horizontal shear and tides, and not by tides alone; for example, tides coherently transport patches of particles back and forth with little dispersion.

The enhancement of dispersion because of submesoscale flow is also seen in the correspondence between cross-shelf patterns in dispersive frequency Q^+ and submesoscale rms velocity fluctuations, whose correlation yields $r^2 = 0.77$ (Figs. 4d,e). As shown in Fig. 4e, the submesoscale flow exhibits stronger fluctuations near headlands compared to embayments. This suggests that the enhanced dispersion near headlands is due to increased submesoscale activity.

The effects of increased submesoscale activity on the two-particle dispersion in the coastal environment are also assessed by comparing the dispersal results simulated with a horizontal grid resolution of 250 m with a higher-resolution simulation (75 m) nested in the southeastern part domain (red box in Fig. 1). The 75-m (L3) domain is simulated only for winter 2007/08 and includes: two bays (SM and HB) and one headland (PV).

Figures 13a,b show $R_a^2(t)$ and $R_c^2(t)$, respectively, for the data bin closest to the shore ($\leq$2 km) comparing the L2 (solid lines) and L3 (dashed lines) simulations with R_o = 150 m. Regardless of direction, the L3 simulation is more dispersive. This effect is more pronounced for bays particularly close to the shore and therefore the data bins farther from the shore are not shown.

The impact of the model horizontal grid resolution on the relative diffusivity is investigated with respect to the distance from the shore and initial particle pair separation. Figure 14 shows the average ratio of the scale-dependent diffusivities $\langle \kappa_a^{\mathrm{L3}}/\kappa_a^{\mathrm{L2}} \rangle$ and $\langle \kappa_c^{\mathrm{L3}}/\kappa_c^{\mathrm{L2}} \rangle$ plotted against L_c in Figs. 14a,c and 14b,d, respectively, with R_o = 500 and 150 m in the top and bottom panels, respectively; where the superscripts L3 and L2 refer to the model configuration, and the angle brackets correspond to an average overall overlapping rms pair separation

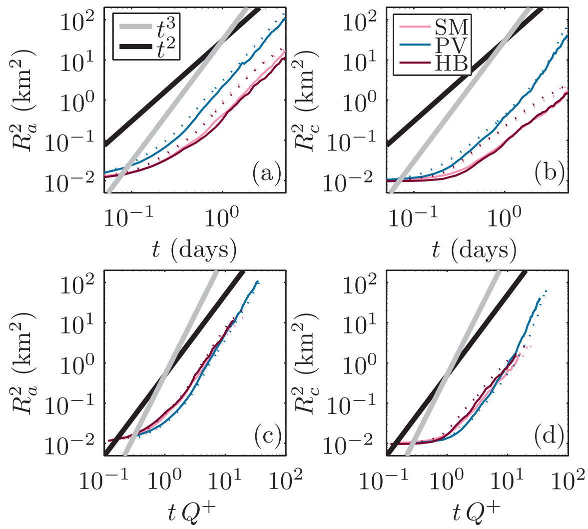

FIG. 13. Mean particle separation–squared R^2 vs time. (a),(c) The along- [$R_a^2(t)$] and (b),(d) cross-shelf [$R_c^2(t)$] components are shown. Time is scaled by the frequency Q^+ in (c),(d). The solid and dotted lines correspond to the simulations with horizontal resolutions of 250 (L2) and 75 m (L3), respectively. The data correspond to particles pairs with R_o = 150 m and center positions from 0 to 2 km from the shore.

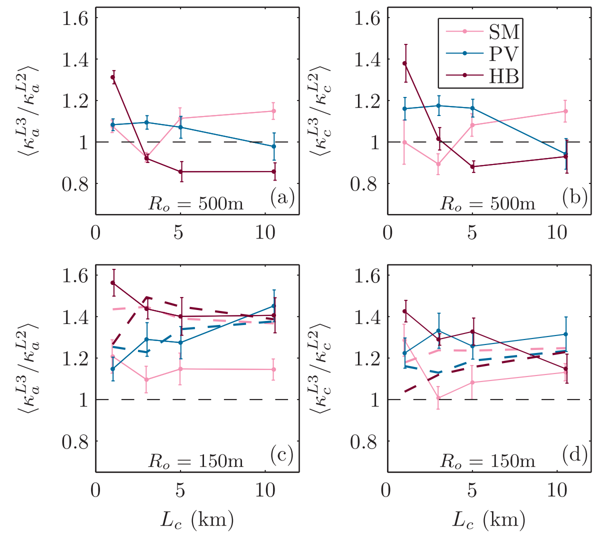

FIG. 14. Mean ratio of the scale-dependent relative diffusivity in the along- and cross-shelf directions plotted against the distance from the shore L_c. The relative diffusivities from the 75- and 250-m resolution model correspond to κ^{L3} and κ^{L2}, respectively. The initial particle pair separation R_o is (a),(b) 500 and (c),(d) 150 m. The brackets correspond to an average over the overlapping rms pair separations between the two datasets. To calculate the ratios between κ^{L3} and κ^{L2}, the scale-dependent diffusivities were bin averaged at scale intervals of 500 m. The error bars correspond to the standard error of the mean. For a valid comparison, the L2-resolution data in this figure only used the particles located within the higher-resolution grid (L3), see model domains in Fig. 1. The dashed lines in (b),(d) correspond to the predictions by the power-law model Eq. (25) and the best-fit coefficients in Eqs. (13)–(19) with the corresponding values of Q^+ and rms velocities.

(not a temporal average; see caption for details). When R_o = 500 m, both models are expected to resolve the eddies between particle pairs. As shown in Figs. 14a,b, under this condition the higher resolution model on average does not produce larger relative diffusivities. In contrast, Figs. 14c,d show that for R_o = 150 m the higher-resolution simulation produces larger relative diffusion by up to 50%. There is a discernible enhancement of the relative diffusivities in L3 for small initial separations that are under resolved in L2. The diffusivity enhancement mostly decreases with increasing L_c for bays, while increasing with L_c for PV.

Following Poje et al. (2010), the parameter Q^+ is used to scale the time of the relative dispersion curves across the two model resolutions. Figures 13c,d show $R_a^2(tQ^+)$ and $R_c^2(tQ^+)$, respectively, from all three regions and the two model resolutions, collapsing into two groups: the along- and cross-shelf directions. This confirms the robustness of Q^+ to characterize the dispersion in the coastal zone.

The scale-dependent power-law model of the relative diffusivity in Eq. (22) provides a way of comparing dispersal characteristics for the two grid resolutions. In dimensional form, Eq. (22) becomes

$$\kappa_i = A_i^{1/B_i} Q^+ \frac{u_{i_{\rm rms}}}{u_{\rm rms}} R^{[2(B_i-1)]/B_i}. \qquad (25)$$

Because Q^+ increases with increased horizontal model resolution, according to Eq. (25) it is expected that the higher-resolution simulation would yield larger scale-dependent diffusivities according to $A_i^{1/B_i}Q^+$. However, as shown in Figs. 14a,b, when R_o = 500 m, both simulations produce similar diffusivities. Taking the best-fit coefficients from Eqs. (13) to (19) and the power-law model from Eq. (25) with the model resolution–dependent Q^+, the predicted-average enhancement of the diffusivities is shown in Figs. 14c,d, compared to the Lagrangian data with R_o = 150 m. The predicted-average ratio of the scale-dependent diffusivity is qualitatively consistent with the Lagrangian data, with largest differences for HB close to the shore. According to Eq. (25), the lack of enhancement on the relative diffusivity with R_o = 500 m suggests that the effective Q^+ that characterizes dispersion corresponds to that at scales comparable to the initial pair separation (i.e., Q^+ from the coarser-model grid). More generally, the analysis suggests that characteristic time scale of dispersion corresponds to $Q^{+(-1)}$ evaluated at the scale of R_o or the model-resolution grid, whichever is largest.

b. Comparison with drifter observations

To our knowledge, the only studies in Southern California of relative dispersion for small-drifter separations are the work by List et al. (1990) and Ohlmann et al. (2012). List et al. (1990) conducted a relative dispersion experiment from six simultaneous drifter trajectories near the ocean surface from two releases (one in the winter and one in the spring) near Point Mateo, which is on the coast about 10 km to the southeast of the easternmost boundary of the L2 model domain. Ohlmann et al. (2012) provided relative dispersion observations from pairs of drifters with initial separation of ~10 m within the Santa Barbara Channel. Neither study reported evidence of anisotropic dispersion; possibly because the drifters were not systematically released close enough to the shore. To compare our results with the observations, we calculate the total relative dispersion $R^2 = (R_a^2 + R_c^2)$ and relative diffusivity $\kappa = (\kappa_a + \kappa_c)$ over all regions combined into two composite sets, bays and headland areas, for each model grid configuration, L2 and L3. Figure 15 shows the composite sets of the total relative diffusivity plotted as a function of the rms particle separation R compared to field observations. The drifter data by Ohlmann et al. (2012) give two regimes, a quadratic dependence (for $R <$ 100 m) followed by a linear dependence. Our model predictions are within the envelope of the data by List et al. (1990) and within the uncertainty associated with the drifter observations by Ohlmann et al. (2012). Our composite averages of the relative diffusivity exhibit a power-law behavior between $\kappa \sim R$ and $\kappa \sim R^{4/3}$, with κ approximately proportional to $R^{5/4}$ for both L2 and L3, regardless of coastal geometry. The composite scale–dependent diffusivity of headlands is always larger than that of bays by up to a factor of 2.5.

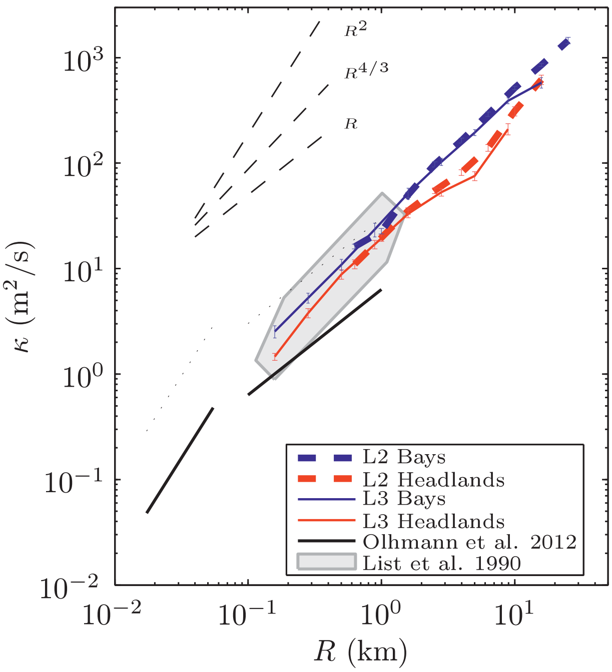

FIG. 15. Total relative diffusivity $\kappa_a + \kappa_c$ as a function of total rms particle separation $R^2 = (R_a^2 + R_c^2)^{1/2}$. The red and blue lines correspond to bays and headland regions, respectively. The envelopes encompassing the L2 simulation data are shown with thin lines. The dashed and solid lines with bars are composite averages corresponding to the L2 and L3 simulation data, with R_o = 500 and 150 m, respectively. The bars are the standard error of the mean. The black solid and dotted lines correspond to the best fits and upper uncertainty, respectively, by Ohlmann et al. (2012) from drifter observations in the Santa Barbara Channel. The area enclosed with gray lines shows the data by List et al. (1990) near San Mateo Point.

c. Kinematics of anisotropic dispersion

Our results show that the flow variance and relative dispersion is increasingly anisotropic closer to the shoreline (Figs. 4c and 7d). We speculate that the anisotropic flow nearshore leads to coherent jets or filaments of vorticity that are generally parallel to the coastline nearshore, and thus may inhibit cross-shelf transport, leading to the retention of particles in the coastal environment (e.g., Largier 2003; McWilliams 2009). This hypothesis is tested with the vertical vorticity field at 10-m below surface. Figure 16a shows an example of the vertical vorticity ζ at 10-m below the sea surface, normalized by the Coriolis parameter f. The data show several vorticity structures with streak-like shapes exceeding values of $2f$ and occasionally reaching $5f$. The streaks shown in Fig. 16a appear to be aligned more in the along- than cross-shore direction.

The contours surrounding large vorticity values ($|\zeta|/f$ = 2 and 5) are fitted to ellipses over the entire duration of the L2 simulations following the work of Romero and Melville (2011). This provides information about the length and orientation of the vorticity structures as well as its ellipticity e defined as the ratio of the minor to the major axis of the ellipse. The dashed-black line in Fig. 16a shows an example of an ellipse fit around a vorticity contour with $\zeta/f = 2$.

A statistical characterization of ellipses fit to structures of large vorticity (i.e., contours of $\zeta/f = \pm 2$, 5) within the coastal region yields many more structures of positive than negative vorticity. On average, 8 times more structures with positive than negative vorticity are found for values of $|\zeta|/f = 5$, and about 3 times more structures with positive than negative vorticity for $|\zeta|/f = 2$. This is because for large values of ζ/f vortex stretching reinforces positive vorticity, while negative

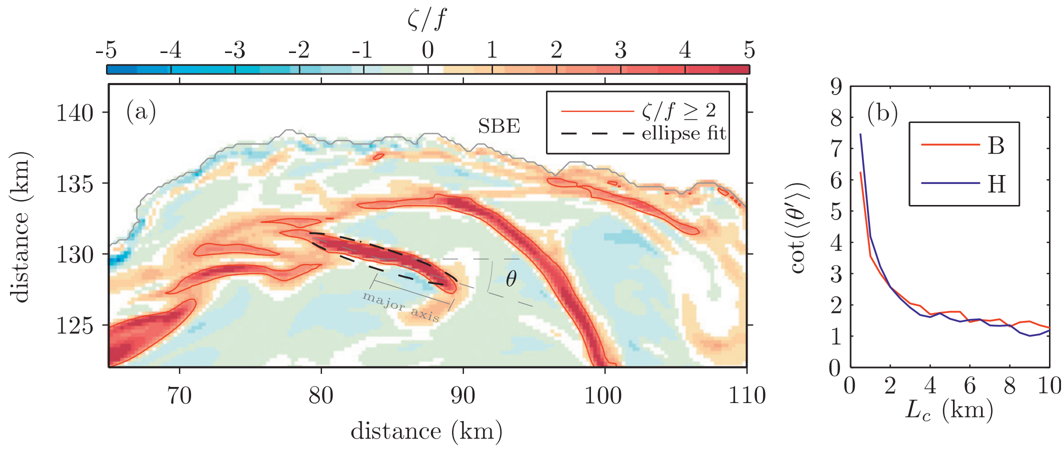

FIG. 16. (a) Sample map of vertical vorticity ζ normalized by the planetary vorticity f near the coast of the East Santa Barbara Channel. The solid red contours correspond to $\zeta/f = 2$. The black-dashed line shows an example of an ellipse fitted to the overlapping red contour. The solid gray line shows the major axis of the ellipse with an orientation θ relative to the horizontal axis. (b) Mean along- to cross-shelf ratio of the alignment of the ellipses fitted over areas where $\zeta/f = 2$ and 5, where θ' is the ellipse orientation relative the shelf (i.e., $\theta' = 0$ is along shelf), and the brackets correspond to a bin average over all ellipses with an offshore bin size of 500 m. The red and blue lines correspond to composite averages of bays and headland regions, respectively.

vorticity is limited by centrifugal instability (Capet et al. 2008a). Also, the ellipse fit analysis yields on average 3.5 times more elliptical ($e < 0.5$) than circular structures, consistently over all the coastal regions. This suggests anisotropy possibly because of fronts and filaments. We focus the analysis on elliptical structures with positive vorticity.

The statistical analysis of the orientation of the ellipses confirms the hypothesis that large vorticity structures are generally aligned with the shelf nearshore and have no preferred orientation offshore. Figure 16b shows $\cot(\langle\theta'\rangle)$ against L_c, where θ' is the orientation of the ellipses relative to the shelf, and the angle brackets represent an average over all bay (red line) and headland (blue) data. The cotangent function was chosen in analogy to the degree of anisotropy introduced earlier in the results section. The $\cot(\langle\theta'\rangle)$ decreases with increasing L_c, implying preferred alignment with bathymetric contours nearshore and nearly random orientation at about 10 km from the shore. This pattern is qualitatively similar to the degree of anisotropy of the average relative diffusivities in Fig. 7d. The ellipse analysis suggests that fronts and filaments are generally aligned with the coast nearshore and are randomly oriented offshore, limiting the cross-shelf transport and dispersion nearshore.

6. Summary and conclusions

A two-particle dispersion analysis within 15 km of the shore from high-resolution ROMS simulations was presented. The numerical simulations have a horizontal grid resolution of 250 m and include tidal forcing and realistic atmospheric surface forcing. The Lagrangian two-particle statistics with initial separations of 500 m are characterized by the coastal geometry, depth, and distance from the shore. Dispersion is dominated by submesoscales, not by tides. The relative dispersion and diffusivity are strongly anisotropic in the nearshore and tend toward isotropy within 10 km of the coast. In general, headlands have larger strain rates, are more energetic and dispersive, and exhibit more submesoscale activity than bay areas.

A modified Okubo–Weiss parameter $1/Q^+$ is shown to be the characteristic time scale for dispersion at short time scales consistent with the results of Poje et al. (2010). Based upon these findings, the parameter $u_{\mathrm{rms}}/Q^+u_{i_{\mathrm{rms}}}$ is shown to be the characteristic time scale for anisotropic dispersion and the time-averaged diffusivities are well correlated with both $u_{i_{\mathrm{rms}}}^2$ and $u_{i_{\mathrm{rms}}}^2 Q^{+(-1)}$. However, the latter scaling is dimensionally consistent and is close in magnitude to the time-averaged diffusivities.

A power-law model of the form $R_i^2 = A_i[Q^+(u_{i_{\mathrm{rms}}}/u_{\mathrm{rms}})t]^{B_i}$ was fit to the relative dispersion data between 1/4 and 4 days. The exponents B_i vary between 1–2.2 and 1.8–2.5 for bays and headlands, respectively, and values of B_i increase with increasing distance from the shore. The scaling factors in the along-shelf direction A_a for both bays and headlands are approximately constant, whereas the cross-shelf direction A_c is proportional to $(u_{\mathrm{rms}}/Q^+)^2$. Thus the along-shelf component of dispersion depends more strongly on Q^+ than the cross-shelf component. The power-law model explains 60% and 80% of the variance of the average diffusivities between ½ and 2 days in the along- and cross-shelf directions, respectively, and predicts a degree of anisotropy qualitatively consistent with the Lagrangian data. The total scale-dependent relative diffusivity is consistent with available surface drifter observations. At time scales greater than 3 days and between 3 and 10 km, the relative dispersion occasionally increased suddenly suggesting a transition into exponential dispersion, possibly as a result of mesoscale straining.

The numerical simulations included the forcing from tides and realistic wind forcing; however, other important processes such as nonhydrostatic internal waves and the effect of surface waves on currents are not included. Surface waves are expected to be significant in the horizontal dispersion near the surface owing to Stokes drift, Langmuir circulation, and wave-breaking transport. These are subjects of future investigations.

This work has important implications for biological–physical interactions such as the transport of larvae and dissolved material from storm runoff, which can also affect humans. The results provide useful information for subgrid-scale parameterizations for coarse-resolution models (e.g., Haza et al. 2012). In particular, the present results are useful for understanding the ''subpatch'' dispersal for mesoscale models of coastal connectivity (e.g., Mitarai et al. 2009). It is critical for future studies to provide supporting field observations that validate the model predictions. This could be accomplished with drifter observations and dye experiments in various coastal environments.

Acknowledgments. We thank Florian Lemarie for generating the meteorological fields, and Jeroen Molemaker and Alexander Shchepetkin for their help developing the modeling capabilities. This study was supported by the Santa Barbara Coastal Long Term Ecological Research program (NSF OCE-0620276 and OCE-1232779). YU and JCM appreciate support from the Office of Naval Research (N00014-12-1-0939), the Orange County Sanitation District, and the National Oceanic and Atmospheric Administration (A11NOS0120029) through the Southern California Coast Ocean Observing System. DAS would also like to acknowledge additional support from the National Science Foundation (OCE-1155813).

REFERENCES

Babiano, A., C. Basdevant, P. Le Roy, and R. Sadourny, 1990: Relative dispersion in two-dimensional turbulence. *J. Fluid Mech.,* **214,** 535–557, doi:10.1017/S0022112090000258.

Bassin, C. J., L. Washburn, M. Brzezinski, and E. McPhee-Shaw, 2005: Sub-mesoscale coastal eddies observed by high frequency radar: A new mechanism for delivering nutrients to kelp forests in the Southern California Bight. *Geophys. Res. Lett.,* **32,** L12604, doi:10.1029/2005GL023017.

Batchelor, G., 1950: The application of the similarity theory of turbulence to atmospheric diffusion. *Quart. J. Roy. Meteor. Soc.,* **76,** 133–146.

Becker, J. J., D. T. Sandwell, W. H. F. Smith, and J. Braud, 2009: Global bathymetry and elevation data at 30 arc seconds resolution: SRTM30 _ PLUS. *Mar. Geod.,* **32,** 355–371.

Bennett, A. F., 1987: A Lagrangian analysis of turbulent diffusion. *Rev. Geophys.,* **25,** 799–822.

Boffetta, G., G. Lacorata, G. Redaelli, and A. Vulpiani, 2001: Detecting barriers to transport: A review of different techniques. *Physica D,* **159,** 58–70, doi:10.1016/S0167-2789(01)00330-X.

——, A. Mazzino, and A. Vulpiani, 2008: Transport of inert and reactive particles. *Transport and Mixing in Geophysical Flows,* J. B. Weiss and A. Provenzale, Eds., Springer, 37–70.

Buijsman, M. C., Y. Uchiyama, J. C. McWilliams, and C. R. Hill-Lindsay, 2012: Modeling semidiurnal internal tide variability in the Southern California Bight. *J. Phys. Oceanogr.,* **42,** 62–77.

Capet, X., J. C. McWilliams, M. J. Molemaker, and F. Shchepetkin, 2008a: Mesoscale to submesoscale transition in the California Current System. Part I: Flow structure, eddy flux, and observational tests. *J. Phys. Oceanogr.,* **38,** 29–43.

——, ——, ——, and ——, 2008b: Mesoscale to submesoscale transition in the California Current System. Part II: Frontal processes. *J. Phys. Oceanogr.,* **38,** 44–64.

——, ——, ——, and ——, 2008c: Mesoscale to submesoscale transition in the California Current System. Part III: Energy balance and flux. *J. Phys. Oceanogr.,* **38,** 2256–2269.

Clark, D. B., F. Feddersen, and R. T. Guza, 2010: Cross-shore surfzone tracer dispersion in an alongshore current. *J. Geophys. Res.,* **115,** C10035, doi:10.1029/2009JC005683.

Cowen, R. K., and S. Sponaugle, 2009: Larval dispersal and marine population connectivity. *Annu. Rev. Mar. Sci.,* **1,** 443–466, doi:10.1146/annurev.marine.010908.163757.

Davis, R. E., 1983: Oceanic property transport, Lagrangian particle statistics, and their prediction. *J. Mar. Res.,* **41,** 163–194.

——, 1985: Drifter observations of coastal surface currents during CODE: The statistical and dynamical views. *J. Geophys. Res.,* **90,** 4756–4772.

——, 1991: Lagrangian ocean studies. *Annu. Rev. Fluid Mech.,* **23,** 43–64.

Dong, C., and J. C. McWilliams, 2007: A numerical study of island wakes in the Southern California Bight. *Cont. Shelf Res.,* **27,** 1233–1248, doi:10.1016/j.csr.2007.01.016.

Döös, K., V. Rupolo, and L. Brodeau, 2011: Dispersion of surface drifters and model-simulated trajectories. *Ocean Modell.,* **39,** 301–310, doi:10.1016/j.ocemod.2011.05.005.

D'Ovidio, F., V. Fernández, E. Hernández-García, and C. López, 2004: Mixing structures in the Mediterranean Sea from finite-size Lyapunov exponents. *Geophys. Res. Lett.,* **31,** L17203, doi:10.1029/2004GL020328.

Drake, P. T., and C. A. Edwards, 2009: A linear diffusivity model of near-surface, cross-shore particle dispersion from a numerical simulation of central California's coastal ocean. *J. Mar. Res.,* **67,** 385–409.

Fischer, H. B., E. J. List, R. C. Y. Koh, J. Imberger, and N. H. Brooks, 1979: *Mixing in Inland and Coastal Waters.* Academic Press, 483 pp.

Flament, P., L. Armi, and L. Washburn, 1985: The evolving structure of an upwelling filament. *J. Geophys. Res.,* **90,** 11 765–11 778.

Harrison, C. S., D. A. Siegel, and S. Mitarai, 2013: The role of filamentation and eddy-eddy interactions in marine larval accumulation and transport. *Mar. Ecol. Prog. Ser.,* **472,** 27–44, doi:10.3354/meps10061.

Haza, A. C., A. C. Poje, T. M. Özgökmen, and P. Martin, 2008: Relative dispersion from a high-resolution coastal model of the Adriatic Sea. *Ocean Modell.,* **22,** 48–65, doi:10.1016/j.ocemod.2008.01.006.

——, T. M. Özgökmen, A. Griffa, Z. D. Garraffo, and L. Piterbarg, 2012: Parameterization of particle transport at submesoscales in the Gulf Stream region using Lagrangian subgridscale models. *Ocean Modell.,* **42,** 31–49, doi:10.1016/j.ocemod.2011.11.005.

LaCasce, J. H., 2008: Statistics from Lagrangian observations. *Prog. Oceanogr.,* **77,** 1–29, doi:10.1016/j.pocean.2008.02.002.

——, and C. Ohlmann, 2003: Relative dispersion at the surface of the Gulf of Mexico. *J. Mar. Res.,* **61,** 285–312.

Largier, J., 2003: Considerations in estimating larval dispersal distances. *Ecol. Appl.,* **13,** 71–89.

Lentz, S. J., and M. R. Fewings, 2012: The wind- and wave-driven inner-shelf circulation. *Annu. Rev. Mar. Sci.,* **4,** 317–343, doi:10.1146/annurev-marine-120709-142745.

Lin, J., 1972: Relative dispersion in the enstrophy-cascading inertial range of homogeneous two-dimensional turbulence. *J. Atmos. Sci.,* **29,** 394–396.

List, E. J., G. Gartrell, and C. D. Winant, 1990: Diffusion and dispersion in coastal waters. *J. Hydraul. Eng.,* **116,** 1158–1179.

Lumpkin, R., and S. Elipot, 2010: Surface drifter pair spreading in the North Atlantic. *J. Geophys. Res.,* **115,** C12017, doi:10.1029/2010JC006338.

McWilliams, J. C., 1984: The emergence of isolated coherent vortices in turbulent flow. *J. Fluid Mech.,* **146,** 21–43.

——, 2009: Dynamics of atmospheres and oceans targeted coastal circulation phenomena in diagnostic analyses and forecasts. *Dyn. Atmos. Oceans,* **48,** 3–15, doi:10.1016/j.dynatmoce.2008.12.004.

Mitarai, S., D. A. Siegel, J. R. Watson, C. Dong, and J. C. McWilliams, 2009: Quantifying connectivity in the coastal ocean with application to the Southern California Bight. *J. Geophys. Res.,* **114,** C10026, doi:10.1029/2008JC005166.

Morel, P., and M. Larcheveque, 1974: Relative dispersion of constant-level balloons in the 200-mb general circulation. *J. Atmos. Sci.,* **31,** 2189–2196.

Nickols, K. J., B. Gaylord, and J. L. Largier, 2012: The coastal boundary layer: Predictable current structure decreases alongshore transport and alters scales of dispersal. *Mar. Ecol. Prog. Ser.,* **464,** 17–35, doi:10.3354/meps09875.

O'Dwyer, J., R. G. Williams, J. H. Lacasce, and K. G. Speer, 2000: Does the potential vorticity distribution constrain the spreading of floats in the North Atlantic? *J. Phys. Oceanogr.,* **30,** 721–732.

Ohlmann, J. C., J. H. LaCasce, L. Washburn, A. J. Mariano, and B. Emery, 2012: Relative dispersion observations and trajectory modeling in the Santa Barbara Channel. *J. Geophys. Res.,* **117,** C05040, doi:10.1029/2011JC007810.

Okubo, A., 1970: Horizontal dispersion of floatable particles in the vicinity of velocity singularities such as convergences. *Deep Sea Res. Oceanogr. Abstr.,* **17,** 445–454.

Ollitrault, M., C. Gabillet, and A. C. De Verdière, 2005: Open ocean regimes of relative dispersion. *J. Fluid Mech.,* **533,** 381–407, doi:10.1017/S0022112005004556.

Poje, A. C., A. C. Haza, T. M. Özgökmen, M. G. Magaldi, and Z. D. Garraffo, 2010: Resolution dependent relative dispersion statistics in a hierarchy of ocean models. *Ocean Modell.,* **31,** 36–50, doi:10.1016/j.ocemod.2009.09.002.

Richardson, L., 1926: Atmospheric diffusion shown on a distance-neighbour graph. *Proc. Roy. Soc. London,* **A110,** 709–737.

Romero, L., and W. K. Melville, 2011: Spatial statistics of the sea surface in fetch-limited conditions. *J. Phys. Oceanogr.,* **41,** 1821–1841.

Schroeder, K., and Coauthors, 2012: Targeted Lagrangian sampling of submesoscale dispersion at a coastal frontal zone. *Geophys. Res. Lett.,* **39,** L11608, doi:10.1029/2012GL051879.

Shchepetkin, A. F., and J. C. McWilliams, 2005: The regional oceanic modeling system (ROMS): Oceanic model. *Ocean Modell.,* **9,** 347–404, doi:10.1016/j.ocemod.2004.08.002.

Signell, R., and W. Geyer, 1990: Numerical simulation of tidal dispersion around a coastal headland. *Coastal and Estuarine Studies, Geophys. Monogr.,* Vol. 38, Amer. Geophys. Union, 210–222.

——, and ——, 1991: Transient eddy formation around headlands. *J. Geophys. Res.,* **96,** 2561–2575.

Spydell, M. S., F. Feddersen, and R. T. Guza, 2009: Observations of drifter dispersion in the surfzone: The effect of sheared alongshore currents. *J. Geophys. Res.,* **114,** C07028, doi:10.1029/2009JC005328.

Swenson, M. S., and P. P. Niiler, 1996: Statistical analysis of the surface circulation of the California Current. *J. Geophys. Res.,* **101,** 22 631–22 645.

Taylor, G., 1922: Diffusion by Continuous Movements. *Proc. London Math. Soc.,* **s2-20,** 196–212.

Washburn, L., and L. Armi, 1988: Observations of frontal instabilities on an upwelling filament. *J. Phys. Oceanogr.,* **18,** 1075–1092.

Waugh, D. W., E. R. Abraham, and M. M. Bowen, 2006: Spatial variations of stirring in the surface ocean: A case study of the Tasman Sea. *J. Phys. Oceanogr.,* **26,** 526–542.

Weiss, J., 1991: The dynamics of enstrophy transfer in two-dimensional hydrodynamics. *Physica D,* **48,** 273–294.